JOURNAL OF GEOPHYSICAL RESEARCH, VOL. 107, NO. B10, 2229, doi:10.1029/2001JB000591, 2002

Fragmentation of a porous viscoelastic material: Implications to magma fragmentation

Mie Ichihara
Shock Wave Research Center, Institute of Fluid Science, Tohoku University, Sendai, Japan

Daniel Rittel
Faculty of Mechanical Engineering, Technion, Israel Institute of Technology, Haifa, Israel

Bradford Sturtevant[1]
Graduate Aeronautical Laboratory, California Institute of Technology, Pasadena, California, USA

Received 29 October 2001; revised 31 December 2001; accepted 4 January 2002; published 15 October 2002.

[1] Fragmentation of vesicular magma by rapid decompression is one of the most likely triggers for explosive eruptions. In this phenomenon the decompression rate and the viscoelastic nature of magma are considered to be key factors. In order to obtain a clear idea on the effects of these two factors, controlled fragmentation experiments have been conducted. These experiments have three advantages. First, the specimen is made of a viscoelastic material with controlled porosity and geometry. Second, the fragmentation process is directly monitored. Finally, both the magnitude and rate of decompression are controlled. Brittle fragmentation and ductile expansion were both observed in the same porous material at different timescales. The various mechanical responses of the specimen (elastic, flow, and fragmentation) were correlated with the pressure profile measured at the base of the specimen. Fragmentation was noted to occur when the decompression exceeded a critical value within a critical time. Two relevant timescales are discussed in terms of physical mechanisms of relaxation. The first is the measured glass transition time. The second is the estimated timescale for the onset of viscous bubble expansion. The observed phenomena bear several similarities with natural magma fragmentation. It is thus considered that the present results are a useful step toward constructing a model for magma fragmentation. *INDEX TERMS:* 8414 Volcanology: Eruption mechanisms; 5104 Physical Properties of Rocks: Fracture and flow; 8429 Volcanology: Lava rheology and morphology; 3210 Mathematical Geophysics: Modeling; *KEYWORDS:* fragmentation, eruption, rheology, experimental volocanology, magma, viscoelasticity

Citation: Ichihara, M., D. Rittel, and B. Sturtevant, Fragmentation of a porous viscoelastic material: Implications to magma fragmentation, *J. Geophys. Res.*, *107*(B10), 2229, doi:10.1029/2001JB000591, 2002.

1. Introduction

[2] Fragmentation of vesicular magma is an essential stage of an explosive eruption. Before fragmentation, the mixture of magma and gas moves slowly, controlled by the viscosity of magma. The explosive force of an eruption is generated during fragmentation, where the potential energy of the magma and compressed gas bubbles is converted into kinetic energy of the violent gas-particle flow. It is considered that there are two ultimate types of fragmentation: one is solid-like brittle fragmentation, and the other is liquid-like ductile fragmentation [*Heiken and Wohletz*, 1985; *Mader*, 1998; *Dingwell*, 1998; *Cashman et al.*, 1999]. The way in which fragmentation occurs plays an important role in determining the intensity and the style of an explosive eruption [*Alidibirov and Dingwell*, 1996, 2000]. Brittle fragmentation can release energy much more efficiently than the ductile process, and the most explosive eruptions are associated with brittle fragmentation [*Heiken and Wohletz*, 1985; *Taddeucci and Wohletz*, 2001; *Kaminski and Jaupart*, 1998].

[3] The present paper investigates brittle fragmentation of vesicular magma by rapid decompression. This process is one of the most likely scenarios to cause a volcanic blast [*Alidibirov and Dingwell*, 2000; *Cashman et al.*, 1999; *Fink and Kieffer*, 1993]. It may also occur in the initial stage [*Wohletz et al.*, 1984], or in the internal process [*Cashman et al.*, 1999] of a Plinian eruption, although the steady characteristics of the eruption are often described with other models such as fragmentation by the rapid acceleration of vesicular magma [*Papale*, 1999] or by interaction between expanding bubbles [*Sparks*, 1978].

[1]Deceased.

0148-0227/02/2001JB000591$09.00

[4] Theoretical models of brittle magma fragmentation after rapid decompression assume the progression of the fragmentation front into the vesicular magma. This assumption is based on shock tube theory [*Turcotte et al.*, 1990; *Wohletz et al.*, 1984], vaporization waves [*Bennett*, 1971], and rock burst phenomena [*Alidibirov*, 1994; *Alidibirov and Dingwell*, 2000]. These models interpret the fragmentation front as a discontinuous boundary which might include a pressure discontinuity. Rupture of the melt phase occurs in the fragmentation front at the micro-scale. At this scale, rapid decompression is regarded as a decisive factor due to the time-dependent mechanical response of silicate melts [*Alidibirov and Dingwell*, 1996, 2000; *Martel et al.*, 2000; *Zhang et al.*, 1997; *Cashman et al.*, 1999]. Silicate melts respond as elastic solid within a finite period of time and behave as viscous fluid on a longer timescale. The transition time between the elastic and viscous response of the melt is called the glass transition time or the relaxation time (subsequently noted t_g) [*Dingwell and Webb*, 1989; *Webb*, 1997]. The onset of non-Newtonian, shear-thinning rheology of magma is observed at strain rates a few orders of magnitude less than the relaxation strain rate, that is, t_g^{-1} [*Webb and Dingwell*, 1990].

[5] Experimental studies on the fragmentation by rapid decompression have been conducted on natural magma and analogous materials. The experiments using natural magma have revealed the nature of magma fragmentation itself. The contribution of the viscoelasticity of the magma to the fragmentation process, the critical magnitude of decompression required to cause fragmentation, and the dependence of the fragment size on the experimental conditions (decompression magnitude, initial void fraction, crystal content, temperature, etc.) have all been reported [*Alidibirov and Dingwell*, 1996; *Martel et al.*, 2000; *Martel et al.*, 2001; O. Spieler et al., Magma fragmentation speed: An experimental determination, submitted to Geophysical Research Letters, 2001, hereinafter referred to as Spieler et al., submitted manuscript, 2001].

[6] On the other hand, the use of analogous materials allows direct monitoring of the fragmentation process without experimental constraints related to high temperature testing. Obvious brittle fragmentation was observed in experiments using a porous solid material [*Alidibirov and Panov*, 1998]. They noted a layer-by-layer fragmentation characterized by fracture planes perpendicular to the decompression axis. These authors also presented the effects of the magnitude of decompression on the fragment size and fragmentation threshold. Their observations have influenced the modeling of brittle fragmentation of vesicular magma. Most of other analogous experiments used liquid-gas systems and observed liquid-like ductile fragmentation, where the bubble expansion and the acceleration of the matrix preceded and caused the fragmentation [*Mader et al.*, 1994; *Sparks et al.*, 1994; *Zhang et al.*, 1997; *Zhang*, 1998]. Other interesting types of fragmentation are observed in experiments using Gum Rosin-Acetone system which simulates the temperature and the volatile-content dependence of the magma viscosity [*Phillips et al.*, 1995], superheated refrigerant [*Hill and Sturtevant*, 1990], and superheated liquid and particles [*Sugioka and Bulsik*, 1995]. However, the fracture process is not regarded as brittle fragmentation either.

[7] A fracture criterion has been proposed in which brittle rupture of magma occurs when decompression time is shorter than t_g and a tensile stress greater than the material strength is applied by the excess pressure in the bubbles [*Alidibirov and Dingwell*, 2000; *Martel et al.*, 2000; *Zhang*, 1999; *Cashman et al.*, 1999] and/or the strain rates of deformation are sufficiently high to drive the melt phase into the non-Newtonian, shear-thinning phase [*Dingwell*, 1996]. Therefore, it is acknowledged that the decompression rate and the viscoelastic nature of magma are key factors in the fragmentation process by rapid decompression. However, their effect has not been yet systematically investigated by experiments, to our knowledge. Consequently, the following basic issues remain to be addressed:

1. How does the porous viscoelastic material behave on rapid decompression?
2. What are the factors responsible for brittle fragmentation of a given viscoelastic material?

[8] The present experiments are designed to answer these questions. Fragmentation experiments were conducted on a viscoelastic compound containing bubbles using a transparent glass shock tube. The rheological properties of the material were measured separately, and the glass transition time (t_g) was determined. The timescale of the decompression in the fragmentation experiment was controlled to include t_g. We observed a clear transition from brittle fragmentation to ductile response of the specimen as the decompression rate decreases. The relation between the critical decompression rate and the rheology of the compound itself is discussed.

2. Experimental Method

2.1. Material and Mechanical Testing

[9] Dilatant silicone compound (Dow Corning 3179) was selected as the experimental material. This material has a well known time-dependent response: when it is stretched slowly, it thins down to thread, while when it is pulled apart quickly, it separates into two pieces with flat sections. Although it is categorized as a viscous fluid by the manufacturer, a ball of the compound can even bounce, when it hits the floor. A similar material, known as ''Silly Putty,' has been commercially available in the United States for some 50 years.

[10] The time-dependent shear modulus is often represented as a complex modulus which is a function of angular frequency ω. The real part $G'(\omega)$ is called dynamic storage modulus and represents the elastic response, and the imaginary part $G''(\omega)$ is called dynamic loss modulus and represents the viscous response. The loss modulus is related to the dynamic viscosity $\eta'(\omega)$ as $\eta'(\omega) = G''(\omega)/\omega$.

[11] Frequency dependence of the dynamic moduli for a typical polymer melt consisting of long linear chains is explained by *Graessley* [1993] and is represented in Figure 1. At the lowest frequencies, $G'(\omega)$ is much smaller than $G''(\omega)$ so that the viscous response dominates. At intermediate frequencies, $G'(\omega)$ is larger than $G''(\omega)$, and the elastic response dominates. The relative magnitudes revert again on entering the transition zone. Eventually, $G'(\omega)$ levels off at the glassy modulus and $G''(\omega)$ falls off again in the glassy zone. The loss modulus has two peaks, corresponding to the relaxation of local structure (at high

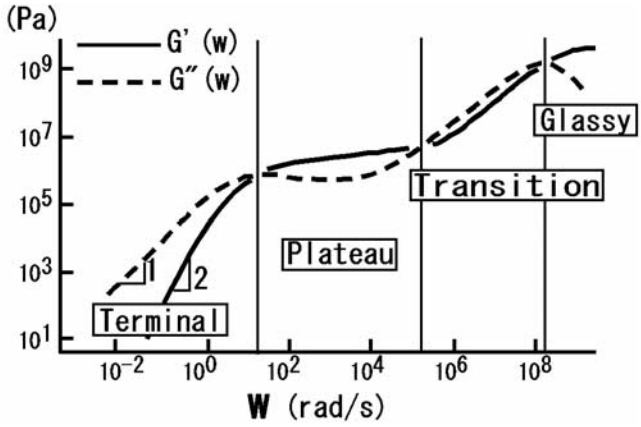

Figure 1. The dynamic storage modulus, $G'(\omega)$, and the dynamic loss modulus, $G''(\omega)$, of a typical polymer melt. Adapted from FIGURE 11 of *Graessley* [1993].

frequency) and the relaxation of large-scale chain structure (at low frequency). Whether the plateau zone exists or not depends on the molecular size and intermolecular structure [*Graessley*, 1993; *Eisenberg*, 1993].

[12] The dynamic shear modulus of the compound was measured by forced torsion oscillations using a stress rheometer (Rheometrics Scientific F.E., SR-5). A disk of material with diameter of 25 mm and thickness of about 1.2–1.3 mm was inserted between two planar plates and sinusoidal torsion strain was applied. By measuring the magnitude and the phase delay of the associated stress, the apparatus automatically returns the dynamic modulus as a function of frequency. The amplitude of the applied strain, 0.1%, has been confirmed to be within the range of linear response of the material. The frequency range of the test was 0.0034–16 Hz. The lower frequency covers the time-scale of the decompression experiment in the range of 0.1 ms to 10 s. The upper frequency is limited by the apparatus. The temperature was fixed at 23°C during the measurement.

[13] In order to assess the elastic response of the material at a higher frequency, ultrasonic test was conducted. Piezo-electric transducers, Panametrics V103 and V153 (resonant frequency 1 MHz), are used for *p* wave and *s* wave measurement, respectively. A pair of transducers were used in transmission mode at various spacing, and the wave velocity was determined from the transfer time of the acoustic wave. The measurement were done at the room temperature, at −20°C, and at 60°C. As noted later, the temperature is not important in this experiment.

2.2. Specimen Preparation

[14] Figure 2 schematically describes the specimen. We made two half columns of the compound with many holes on the flat surface. Each half column has a diameter of 25.4 mm, a length of about 63 mm, and a porosity of about 50 vol %. After being frozen in dry ice, the porous half columns were filled with crushed dry ice. While still cold, the two halves were put together and introduced into the cylindrical glass tube from the bottom. In order to improve the specimen to tube fitting, a membrane made of the same compound was inserted between the two half columns. The frozen specimen was solid enough to be inserted into the tube without any significant deformation. The void volume fraction remained constant throughout the preparation stage until the decompression test.

[15] Glycerin was applied at the interface between the specimen and the glass wall as a lubricant in most of the experiments. As soon as the specimen was inserted, the bottom of the glass tube was closed. As the dry ice sublimated, the pressure in the tube increased. Due to the slow pressure increase and specimen hardness, the excess gas in the pores could escape through the gap between the pieces of the specimen without causing significant deformation. After reaching the test condition, the pressure was kept constant by releasing the extra gas.

[16] After all the dry ice sublimated and the specimen warmed up to room temperature, perfect sintering of the two specimen halves was observed. Although temperature was not controlled in the experiment, the room temperature was always around 22–23°C.

2.3. Experimental Apparatus

[17] Figure 3 is a sketch of the experimental apparatus [*Hill*, 1991; *Howard*, 1996]. The apparatus mainly consists of a high-pressure section and a low-pressure tank separated by a diaphragm. The high-pressure section is made of several pyrex glass tubes with an internal diameter of 25.4 mm and a length of about 600 mm in total. The low-pressure tank has a volume of 0.27 m^3, which is much larger than the volume of the high-pressure section. A diaphragm cutter assembly is mounted in the tank and driven by a solenoid valve.

[18] An aluminum orifice with various opening diameters of 2.4–6.4 mm is inserted at the connection of the two glass

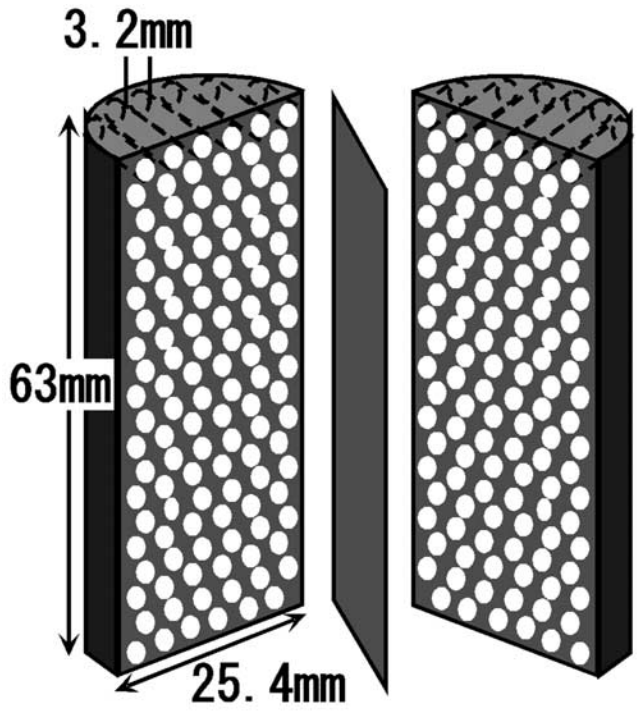

Figure 2. Structure of the specimen made of the viscoelastic compound (Dow Corning 3179). The void fraction is about 50 vol %.

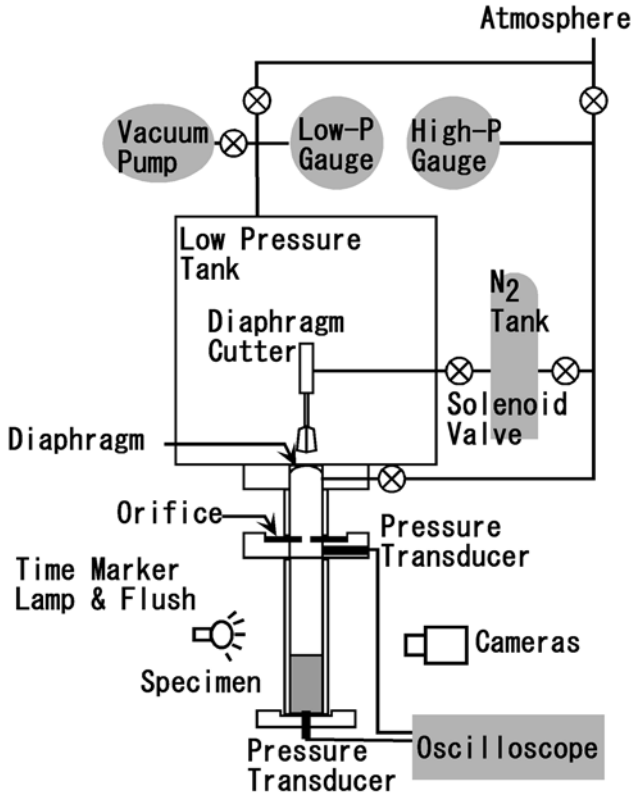

Figure 3. The experimental apparatus.

tubes in order to control the decompression rates. For the largest decompression rate, the orifice is removed and a net is inserted so as to prevent the fragments from flying into the vacuum tank. The initial tank pressure was 4 kPa in all the experiments, and the initial pressure in the test section was either 510 kPa or 300 kPa.

[19] Pressure is measured by two piezoelectric transducers (PCB model 113A26) with a resonant frequency of 400 kHz and a discharge time constant of 50 s. One transducer is mounted at the base end and stuck into the specimen. Good contact between the specimen and the transducer is attained without any additional coupling fluid. The other transducer is mounted on the tube wall 10 mm below the orifice. Decompression rate measured at this location is in good agreement with that measured at the bottom of the tube without specimen, so that the upper transducer signal is regarded as the applied decompression to the specimen.

[20] The surface of the upper transducer is covered with silicone rubber to minimize the effect of temperature drop induced by the sudden decompression on the sensitivity of the transducers. Comparing the data taken before and after the transducer is covered, it was observed that the thermal effect is insignificant in the present experiments. The transducer outputs are amplified by a PCB amplifier (model 482A04) and recorded on a Nicolet 4094C digital oscilloscope at the sampling rates of 5–50 kHz.

[21] Frontal illumination of the test section was provided by three 1000-watt type-FCM photoflood lamps (Berkey Colortran model 104-051 fixture). Motion pictures were taken at a rate of 3000 frames per second (fps) using Hycam II manufactured by Redlake Corporation and 16-mm black and white negative film (Kodak 7222, ASA 200). After the experiment, the motion picture was transferred into digital video for the convenience of analyses. The actual time between the frames of the digital video is 4/15 ms. A 100-foot roll of negative film can record motion pictures for about 1 s. Observation of the longer timescale was made by a CCD video camera (Sony DXC-107A) at a rate of 30 fps.

[22] A flash lamp and a flood lamp were used to obtain time correlation between the image and the pressure data. A trigger signal was sent from Hycam II to the diaphragm cutter, the oscilloscope, and the lamps at the same time. In this system, time correlation with a 1-ms accuracy was obtained between the images and the pressure data.

3. Results

3.1. Physical Properties of the Experimental Material

[23] The dynamic modulus of the compound without bubbles obtained by the means described in section 2.1 is presented in Figure 4. The solid and open circles are the storage and the loss moduli measured by the stress rheometer. The two curves are similar to the transition and glassy regimes of Figure 1. The time corresponding to the glass transition, t_g, is 0.3 s. Because the frequency and the rigidity at this point are still much smaller than the typical values presented in Figure 1 [*Graessley*, 1993; *Eisenberg*, 1993], the transition may not yet be the real glass transition. However, the important point is that the viscosity-dominated response of the material turns into the elastic response in this timescale.

[24] From the ultrasonic test, the *p* and *s* wave velocities are determined as 1000 and 54 m/s, respectively. The *p* wave velocity was measured with transducer spacing ranging from 10 to 27 mm. The pulse width was 0.002 ms, so that the wavelength is calculated as 2 mm. The transducer

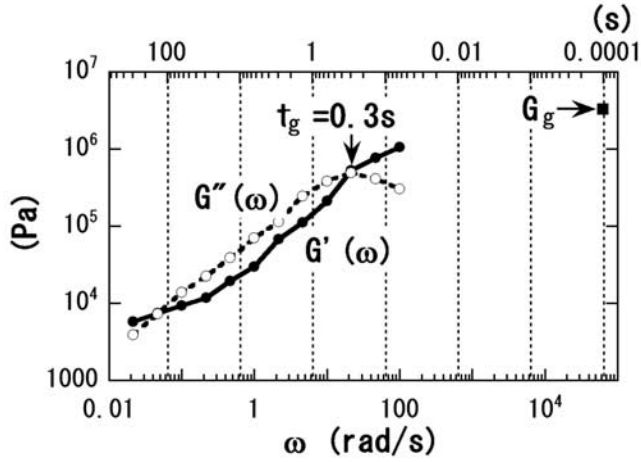

Figure 4. The dynamic storage modulus, $G'(\omega)$ (solid line), and the dynamic loss modulus, $G''(\omega)$ (dotted line), of the test material as functions of the angular frequency, ω. The circles represent data measured by forced torsion oscillation. The point where $G'(\omega)$ overtakes $G''(\omega)$ is defined as the glass transition according to the similarity between these curves and those in Figure 1. The solid square is the shear modulus determined by the ultrasonic test and is regarded as the glassy modulus, G_g.

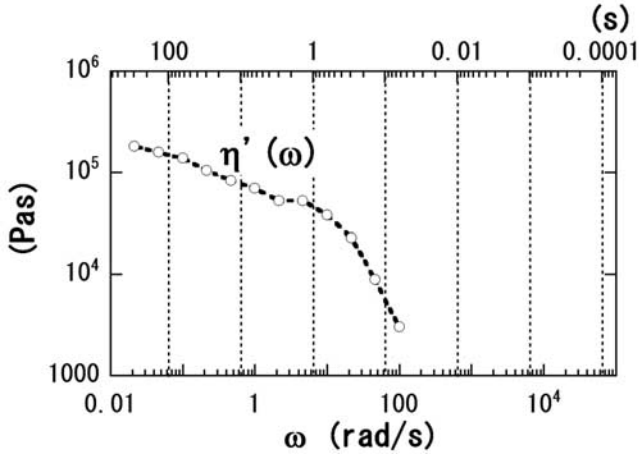

Figure 5. The dynamic shear viscosity, $\eta(\omega)$, of the test material as a function of the angular frequency, ω. The data are calculated using $G''(\omega)$ in Figure 4 by $\eta(\omega) = G''(\omega)/\omega$.

spacings in the *s* wave measurement were in the 5–15 mm range. The pulse width was 0.1 ms, so that the estimated wavelength is 5.4 mm. In both cases, the lateral dimension of the sample was larger than the transducer spacing and the wavelength, so that the three-dimensional effect is not considerable.

[25] It is assumed that the propagation velocities of such short-period waves represent the constant glassy moduli. The *p* and *s* wave velocities are related to the moduli as $\sqrt{(K_g + \frac{4}{3}G_g)/\rho}$ and $\sqrt{G_g/\rho}$, respectively, where K_g is the glassy bulk modulus, G_g is the glassy shear modulus, and ρ is the density. Using $\rho = 1140$ kg/m^3, which is supplied by the manufacturer, we determined $G_g = 3.3$ MPa and $K_g = 1.1$ GPa.

[26] The moduli hardly depend on the temperature in the range from -20 to 60°. Because a change in the temperature of a polymeric material shifts the viscoelastic function along the timescale without a change in shape [*Graessley*, 1993], the constant moduli over the range of temperatures are interpreted as constant moduli over a corresponding range of frequencies at a fixed temperature, even though this frequency range is not known.

[27] The value of G_g is plotted in Figure 4 with a solid square at the frequency corresponding to the pulse width of the *s* wave pulse. One may suppose that the storage modulus asymptotically approaches G_g in the time range between 0.1 s and 0.0001 s. This result is consistent with the assumption that the material response is glassy in the time range shorter than t_g.

[28] The measured loss modulus is translated into the dynamic viscosity in Figure 5. The viscosity in the viscous domain is of order of 10^5 Pa s. It is noted that the shear-thinning rheology is dominant in the time range shorter than 1 s, even though it is observed all over the test ranges.

3.2. Fragmentation Experiments

[29] All the experimental details are listed in Table 1. Two parameters are introduced here to characterize the decompression. The first is the magnitude of the decompression, Δp_o, which is the initial pressure difference between the high and the low pressure sections. The other is the decompression rate, $|\dot{p}|_o$, and defined as the absolute value of the initial pressure gradient outside the specimen. It is calculated from the signal of the upper transducer for the first 10 ms after decompression starts. The reason is that the pressure signal in a long time range is not reliable due to discharge of the transducers. The pressure profile of the upper transducer has exponential characteristics and are basically described by these two parameters, as discussed later.

[30] CCD video images in Figure 6 present typical response of the specimen to large (Figure 6a, 51.4 MPa/s), medium (Figure 6b, 2.72 MPa/s) and small (Figure 6c, 2.64 MPa/s) decompression rates. Because the trigger time has not been marked in these examples, a selected frame before any motion is observed is denoted as time zero. In Figure 6a with a large decompression rate, the specimen broke into several pieces, and each piece flew upward with a large velocity. The rupture surfaces were perpendicular to the decompression axis, and the initial pore shapes were identified on the surfaces as shown in Figure 7, which was obtained at the similar decompression rate (49.4 MPa/s). The fragmentation process took only a few tens of milliseconds, and little deformation was observed before and during it. The length of the fragments was greater than the initial pore radius, so that they still contained high-pressure pores.

[31] In the medium case (Figure 6b), fragmentation still occurred, but the fragmentation process lasted longer. A slight elongation of the specimen was noted in the process. When the decompression rate was decreased to 2.64 MPa/s (Figure 6c), fragmentation ceased to occur. Ductile expansion of the specimen was observed with all the decompression rates (Figures 6a–6c) in a timescale of a few seconds.

[32] Figure 8 summarizes the observation of fragmentation (solid points) and its lack (open points) in a plane of the two condition parameters, Δp_o, and $|\dot{p}|_o$. Figure 8 shows that there is a critical decompression rate above which the fragmentation occurs. Moreover this critical rate does not depend on Δp_o.

[33] The pressure data for the three examples in Figure 6 are plotted in Figure 9. Figure 9a presents the signal of the upper transducer, which is the prescribed decompression, and Figure 9b presents the signal of the bottom transducer. Although the difference in the applied decompression was

Table 1. Experimental Conditions

ID	High *p*, kPa	Δp_o, kPa	Orifice Diameter, mm	$\lvert\dot{p}\rvert_o$, MPa/s
080902	510	506	25.4	49.4
081003			25.4	49.4
081004			25.4	51.4
092804			3.57	4.17
092805			3.57	4.19
081605			3.18	3.30
081608			3.18	2.72
082103			2.78	2.63
082104			2.78	2.64
081606			2.38	1.59
081607			2.38	1.47
082105	300	296	6.35	7.43
082106			3.97	2.88
082107			3.57	2.36
082101			3.18	1.84
082102			3.18	1.95

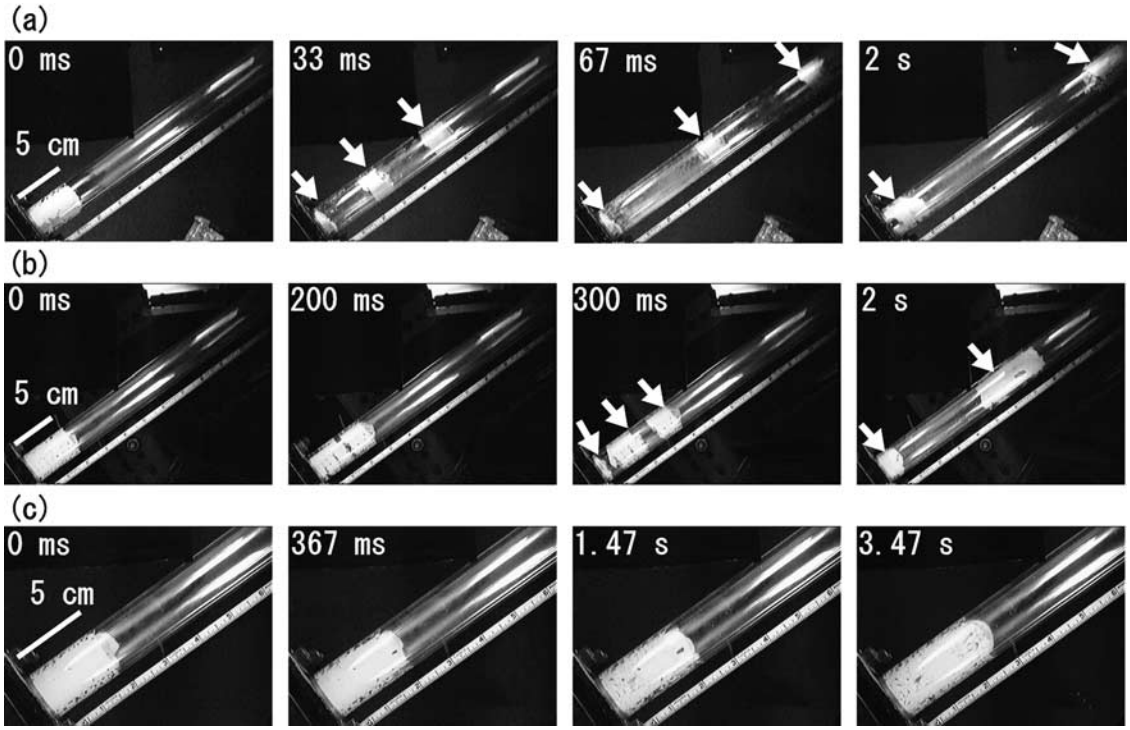

Figure 6. Response of the specimen after decompression at rates of (a) 51.4 MPa/s, (b) 2.72 MPa/s, and (c) 2.64 MPa/s. The arrows indicate the individual fragments. The images are taken by the CCD video camera. A selected frame before any motion is observed is denoted as time zero.

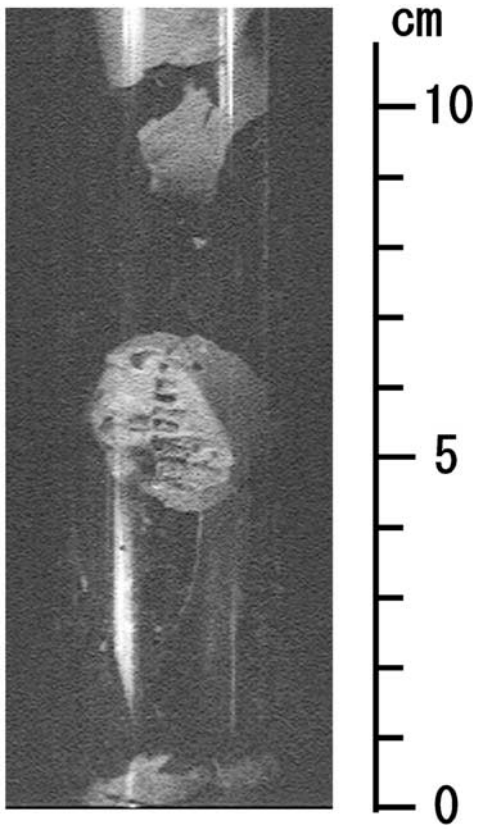

Figure 7. A picture of fragments taken about 20 ms after fragmentation due to rapid decompression at a rate of 49.4 MPa/s. The initial pore structure is seen on the rupture surface.

quite similar between $|\dot{p}|_o$ = 2.72 MPa/s and 2.64 MPa/s, the bottom signals are quite different. A sharp pressure drop was observed at the bottom in the case of $|\dot{p}|_o$ = 2.72 MPa/s as well as the more rapid case, $|\dot{p}|_o$ = 51.4 MPa/s, while the bottom pressure decreased very slowly in the case of $|\dot{p}|_o$ = 2.64 MPa/s.

[34] The fragmentation processes and the associated pressure change were studied in detail using the high-speed motion pictures. The results are shown in Figure 10 for the

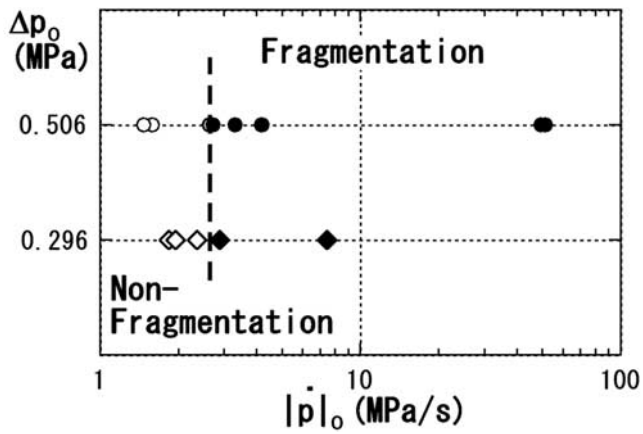

Figure 8. The observation of fragmentation and its lack are indicated by solid points and open points at the corresponding magnitude and rate of decompression, Δp_o and $|\dot{p}|_o$, respectively. Fragmentation occurred at decompression rates larger than the dashed line.

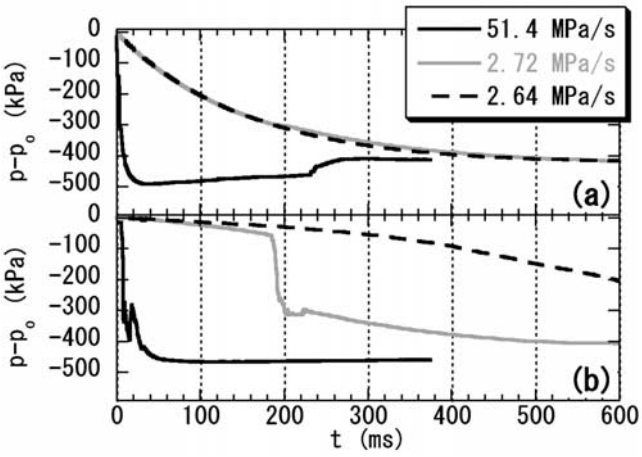

Figure 9. The pressure data measured (a) above the specimen and (b) at the base of the specimen. The data for the decompression rates 51.4 MPa/s (black solid line), 2.72 MPa/s (gray solid line), and 2.64 MPa/s (black dashed line) are the pressure change in experiments in Figures 6a, 6b, and 6c, respectively.

highest decompression case ($|\dot{p}|_o$ = 49.4 MPa/s) and in Figure 11 for the medium decompression case ($|\dot{p}|_o$ = 4.19 MPa/s).

[35] In Figure 10, the time marker was not recorded in the motion pictures. However, the sharp decompression wave produced visible perturbation on the specimen surface within 1 ms after it hit the specimen. This fact was confirmed by later experiments, in which the time marking was successful. Therefore the first frame which showed perturbation on the upper surface of the specimen was regarded as the arrival time of the decompression wave. Because the travel time of the decompression wave between the upper transducer and the surface of the specimen is known, time correlation between the motion pictures and the pressure data was established with an error of 1 ms.

[36] The following sequence of events can be identified during the fragmentation process.

1. The decompression wave was noted to reach the surface of the specimen in Figure 10a, even though it is difficult to see the motion in the still image.

2. No noticeable deformation was observed between Figures 10a and 10b. A small precursor signal was detected by the bottom transducer at 0.73 ms after the time of Figure 10a. The bottom pressure decreases only slightly until Figure 10b.

3. Both the strain rate and decompression rate at the bottom of the specimen increase after Figure 10b.

4. The first cracks appear at the sidewall of the specimen in Figure 10d. The number of cracks increases from 1 in Figure 10d to 4 in Figure 10g. The decompression rate at the bottom of the specimen increases further during this stage.

5. There is a bump in the bottom transducer signal at Figure 10g, but no particular phenomena are noted in the images.

6. The specimen is completely fragmented by Figure 10h, and acceleration of the fragments starts. The bottom pressure continues to decrease during the acceleration process.

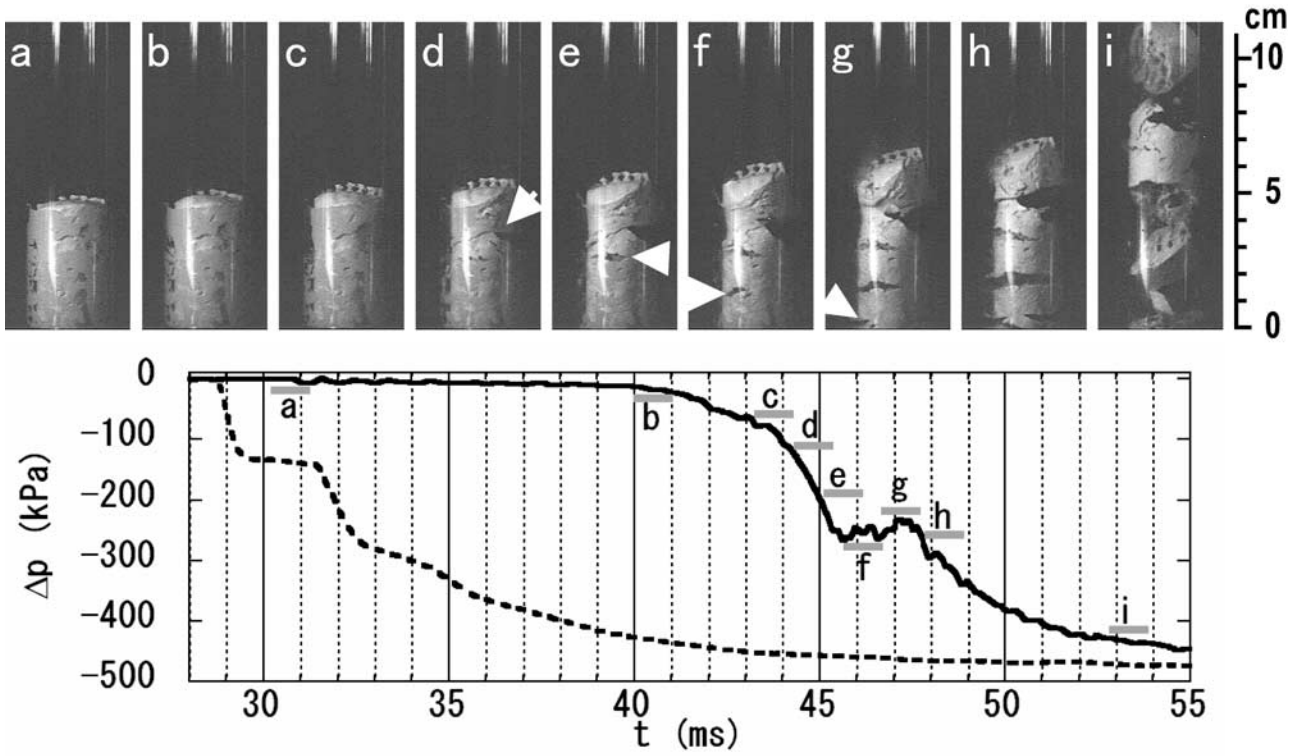

Figure 10. The response of the specimen for the decompression at a rate of 49.4 MPa/s is compared with the pressure data. The pressures above and beneath the specimen are plotted with dashed and solid lines, respectively. The times of the pictures are marked on the bottom pressure curve with accuracy of 1 ms. The arrows point to the incipient fractures.

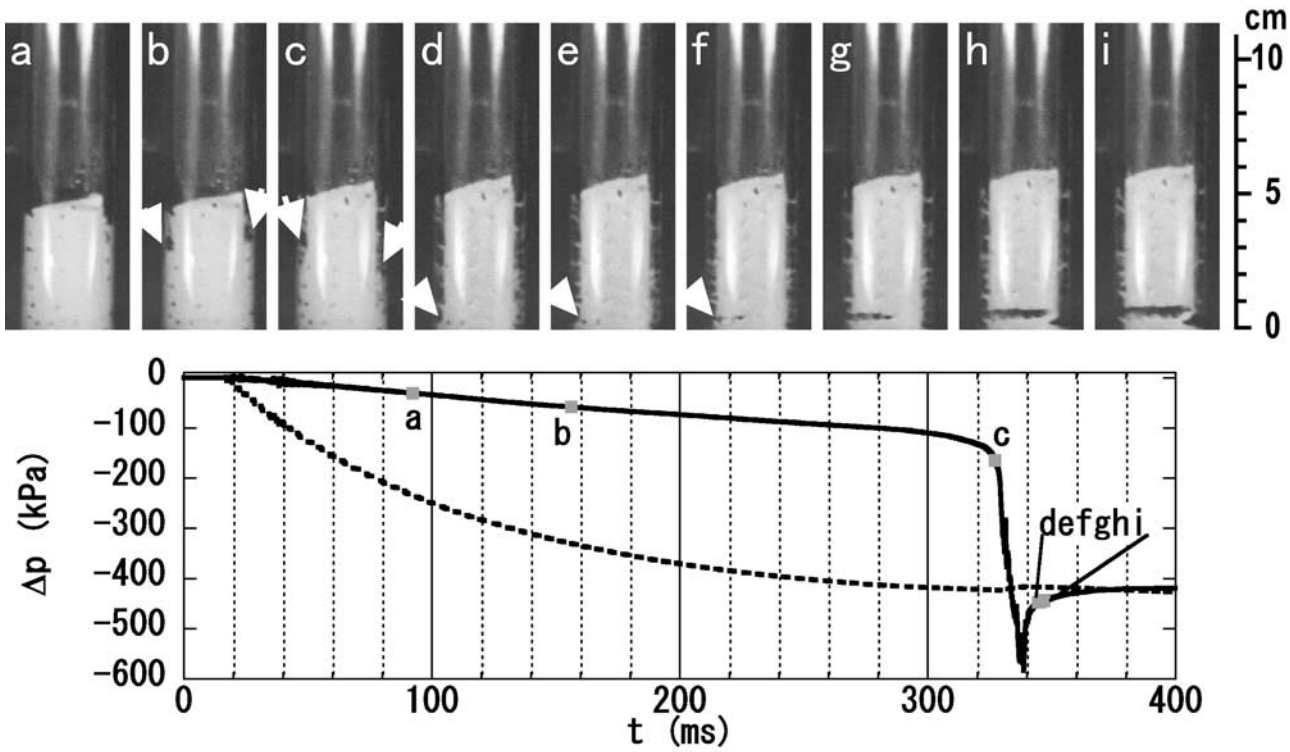

Figure 11. The response of the specimen for the decompression at a rate of 4.19 MPa/s is compared with the pressure data. The pressure above and beneath the specimen are plotted with dashed and solid lines, respectively. The points marked on the curve for the bottom pressure indicate the times of the corresponding pictures. The error of time correlation between the images and the pressure curve is less than 0.33 ms. The arrows on and Figures 11b and 11c point to the front of longitudinal deformation of the specimen, and those on Figures 11d–11f point to growing voids.

[37] In Figure 11, triggering time was marked by the flashlight, so that the error of time correlation between the motion pictures and the pressure data is less than the frame interval, 0.33 ms.

1. Because of the slow decompression, no movement is observed until Figure 11a almost 100 ms after decompression started. The same precursor signal described in the previous example was noted in the slowly decreasing bottom pressure some 0.68 ms after the decompression wave reached the specimen at $t = 18.12$ ms.

2. Longitudinal strain then develops and progresses downward as evidenced from the shoulder in the specimen indicated by the arrows at Figures 11b and 11c, where the specimen diameter is decreasing and its length is increasing.

3. The specimen completely loses contact with the glass wall due to the decrease in the diameter at Figure 10d. Here the shoulder is no longer observed. At the same time, the bottom pressure rapidly decreases and even overshoots.

4. During Figures 11d and 11e, the strain rate suddenly increases, and two voids indicated by the arrows are observed on the lower sidewall of the specimen.

5. The voids become cracks at Figure 11f, and the specimen is fractured by this single crack.

6. The fragmentation process from Figure 11d to 11i occurs in 2.4 ms, which is the same timescale as the fragmentation process in Figure 10.

[38] For the sake of comparison, decompression experiments were conducted with an identical nonporous specimen. The specimen was hardly deformed or ruptured even at the greatest decompression rate. The pressure data are presented in Figure 12. The decompression condition is same as Figure 10. Two important observations can be made.

1. The upper and the bottom transducer signals demonstrate that the decompression wave front propagates through the specimen without any major change. This similarity coincides with the observation that the specimen does not deform, at least as assessed visually. This response is to be contrasted with the observed transition from slow to rapid decompression at the base of the porous specimen (around Figures 10c, 10d, 11c, and 11d), which was observed to

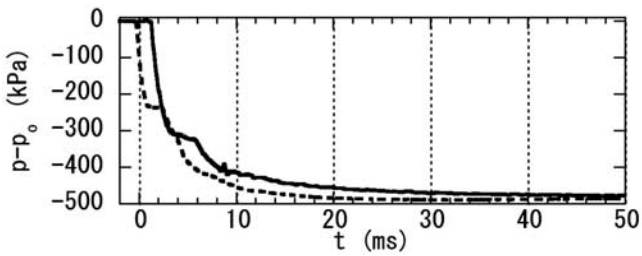

Figure 12. The pressure data for rapid decompression of nonporous specimen. Pressure changes above and beneath the specimen are plotted with dashed and solid lines, respectively.

coincide with the onset of fracture or significant deformation of the specimen according to the decompression rate.

2. Using the known length of the specimen and the travel time of the decompression wave between the upper transducer and the specimen top, the wave velocity in the specimen was estimated as 730 m/s. This value is comparable with the p wave velocity measured by ultrasonic test, which was 1000 m/s. The decompression wave velocity was slightly smaller than the latter, which may be due to the existence of small voids or some nonlinear effects related to the larger amplitude of this wave with respect to the ultrasonic wave. It should be reminded that Figure 12 concerns the compound without bubbles.

[39] Finally, one may wonder about the effect of the glass wall in all these experiments. All the experiments presented above were done with application of lubricant between the specimen and the glass wall. Without the lubricant, the specimen adheres to the wall and the boundary condition becomes quite different. Even then, the essential nature of the phenomena is not different. Namely, the critical decompression rate for fragmentation exists, and the pressure change at the bottom of the specimen correlates with the fragmentation process on rapid decompression. The pressure drop at the bottom of the specimen presented in Figure 11 was due to the loss of contact between the wall and the specimen and was obviously affected by the wall. At the similar decompression rate, the sticky boundary condition can cause fragmentation. Either of systematic measurements or quantitative analyses on the sidewall effect have not been done yet.

4. Discussion

[40] The fragmentation behavior of the porous viscoelastic specimen was presented in the previous section. The following two issues are of particular interest and will therefore be discussed here. First, our results show that there exists a fragmentation threshold, which is determined by the decompression rate and which is independent of the total magnitude of decompression. Second, the pressure change below the specimen is obviously related to the presence of pores and to fragmentation or deformation of the specimen.

[41] In this section, the underlying mechanism responsible for the fragmentation threshold is discussed, first. Three relevant timescales are addressed. These are the critical timescale of decompression to cause fragmentation, t_{cr}, and two additional timescales related to glass transition, t_g, and bubble expansion, t_v. Next, the pressure signal is analyzed in detail. Finally, the implications of the present results in relation to the previous works are described.

4.1. Fragmentation Threshold

[42] We would now like to relate the critical decompression rate to the characteristic time of the material. Because of its exponential characteristics, the applied decompression, $\Delta p(t)$, can be represented using the two parameters, Δp_o and $|\dot{p}|_o$ as

$$\Delta p(t) = p_o - p(t) = \Delta p_o (1 - e^{-t|\dot{p}|_o/\Delta p_o}), \qquad (1)$$

where p_o and $p(t)$ are the pressure in the test section at time zero and t, respectively.

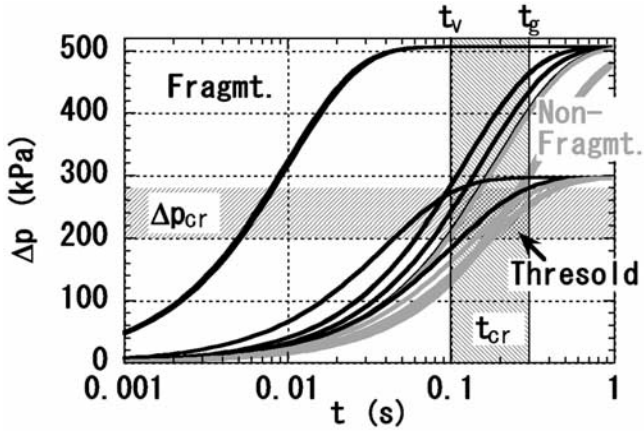

Figure 13. The pressure difference between inside and outside the specimen as a function of time. The curves are obtained using equation (1). The cases in which fragmentation did and did not occur are distinguished by black and gray lines, respectively. The glass transition time of the material (t_g) and the time for onset of viscous expansion (t_v) are shown. The critical decompression magnitude (Δp_{cr}) and the critical decompression time (t_{cr}) to cause the fragmentation are determined using this figure.

[43] The decompression profiles for all the experiments are calculated using equation (1) with the parameters in Table 1, and plotted in Figure 13 as a function of time. In Figure 13 the cases in which fragmentation did and did not occur are distinguished by black and gray lines, respectively.

[44] It is noted that in the time range on the left side of the shaded area ($t < 0.1$ s) almost all the black lines increase faster and reach the shaded range of Δp earlier than the gray lines, regardless of the total magnitude of decompression. Black and gray lines sometimes overlap in the hatched area ($0.1 \leq t \leq 0.3$ s). The black and gray lines are no longer distinct in the longer time range ($t \geq 0.3$ s). It is thus postulated that the hatched area represents the critical time and magnitude of decompression, which we denote by t_{cr} and Δp_{cr}, respectively.

[45] It is proposed that the decompression should reach Δp_{cr} in a time range shorter than t_{cr} to cause fragmentation. The data indicate that $t_{cr} \sim 0.1$ s and $\Delta p_{cr} \sim 200$ kPa. It can reasonably be assumed that Δp_{cr} reflects the strength of the wall of the pores. In the time range of t_{cr}, the observed expansion of the specimen is very small and the loss of the pore gas by permeable flow is expected to be small, too. Therefore, the pressure difference between the inside of the pores and the outside of the specimen should approximately be same as $\Delta p(t)$.

[46] In previous experiments, the fragmentation threshold has been noted only in terms of the critical magnitude of decompression [*Alidibirov and Panov*, 1998; *Martel et al.*, 2000; Spieler et al., submitted manuscript, 2001], even though the existence of the critical decompression time had been suggested [*Alidibirov and Dingwell*, 2000; *Martel et al.*, 2000, 2001; *Zhang*, 1999; *Cashman et al.*, 1999]. Both the critical time and magnitude of the decompression were determined here. It is thus concluded that both the decompression rate and magnitude dictate the nature of the fragmentation process.

4.2. Glass Transition and Bubble Expansion

[47] The glass transition time of the compound has been determined by the rheometer measurement as $t_g = 0.3$ s. It should be noted that t_g is of the same order as the critical decompression time for the fragmentation, $t_{cr} \sim 0.1$ s. The small difference between 0.3 s and 0.1 s cannot be examined with a finer resolution in the present experiments.

[48] One additional relevant timescale, t_v, is determined by the expansion of a bubble. Stress in the matrix due to the excess pore pressure is released in this timescale. Namely, the bubble expansion can keep up with the decompression, if its timescale is larger than t_v, and little excess pressure is stored in the bubbles. It is noted that t_v is determined by the bubble dynamics and different from t_g, although they are sometimes equated with each other.

[49] Volume change of an individual bubble in the foam is formulated by representing the bubble by a single spherical shell [*Prousevitch et al.*, 1993; *Zhang*, 1999]. Although non-Newtonian property is indicated for the present material by the frequency-dependent viscosity (Figure 5) and the pore is not strictly spherical, a rough estimate of t_v is made by an equation of motion for a spherical shell in a Newtonian viscous fluid:

$$\frac{p_o V_o}{V} - p_{out} - \frac{4}{3}\eta(1-\phi)\frac{\dot{V}}{V} = 0, \tag{2}$$

where p_o and V_o denote the initial pressure and volume inside the shell, p_{out} is external pressure, η is the viscosity, ϕ is the void fraction, and V is the inner volume of the shell [*Prousevitch et al.*, 1993]. The first term represents the inner pressure with the assumption of isothermal process. The inertial terms and the effect of the surface tension have been neglected. For the initial stage of the expansion, p_{out} is neglected compared with the first term, and it is assumed that ϕ is constant. Then one obtains

$$\frac{V}{V_0} = \frac{3p_o}{4(1-\phi)\eta}t + 1. \tag{3}$$

Equation (3) indicates that the timescale of the initial expansion is $t_v = 4(1-\phi)\eta/(3p_o)$. It is estimated that $t_v < 0.1$ s for the experimental condition where $\phi = 0.5$, $p_o = 3 - 5 \times 10^5$ Pa, and $\eta < 5 \times 10^4$ Pa s. The range of the viscosity is estimated from Figure 5 with consideration of the timescale of the phenomenon. This result, $t_v \sim t_{cr}$, suggests the possibility that t_{cr} is determined by the timescale of bubble expansion rather than t_g. The numerical solution of equation (2) with variable ϕ and $\eta = 5 \times 10^4$ Pa s indicates that the void expansion is almost completed in 1 s. We have actually observed that ductile expansion of the specimen completed in a few seconds, which is in the same order as the calculation. It is noted that the ductile expansion was observed irrespective of the initial fragmentation process, as long as the timescale was of the order of the second. Because permeable gas escape contributes to release of the excess pore pressure, the total amount of expansion in the experiments is much smaller than the calculation.

[50] The timescale t_v is also related to the initial strain rate of the bubble wall, $\dot{\epsilon}_{rr}$, by the following relation:

$$\dot{\epsilon}_{rr} = \frac{2\dot{R}}{R_o} = \frac{2}{3}\frac{\dot{V}}{3V_o} = \frac{2}{3}t_v^{-1}. \tag{4}$$

The strain rate ($2/3t_v^{-1} > 70\ \text{s}^{-1}$) is larger than the relaxation strain rate ($t_g^{-1} = 30\ \text{s}^{-1}$). It is indicated that the viscous expansion occurs in the shear-thinning phase of the putty.

[51] It is emphasized that the two timescales, t_g and t_v, are associated with different relaxation processes and not always in the same order. The former, t_g, represents the relaxation time of the structure of the viscoelastic fluid, and is determined by the ratio of the viscosity to the rigidity of the fluid. The latter, t_v, represents the relaxation time of the excess pore pressure by viscous expansion of the bubble, and depends on the ratio of the viscosity to the pore pressure. Because the pressure and the rigidity of the test fluid are similar, t_g and t_v are similar in the present condition. The rigidity of magma is of order of 10^{10} Pa [*Webb*, 1997] and is much larger than the realistic pore pressure, which is of order of 10^7 Pa [*Eichelberger and Hayes*, 1982; *Sato et al.*, 1995]. In a case of magma with viscosity of 10^7 Pa s, for example, $t_g < 1$ ms, while $t_v \simeq 1$ s.

[52] The present experiment has suggested the possible connection between t_{cr} and t_g or t_v, but cannot identify which mechanism determines the fragmentation threshold. It is noted that the identification is significant in order to give a fragmentation criterion for magma. Additional experiments using magma itself or analogous material should shed additional light on the relative relevance of t_g and t_v to the fragmentation process.

4.3. Pressure Profiles

[53] Pressure data are analyzed in detail, because pressure change within the specimen is important in building a mathematical model of the phenomena. A small precursor signal was noted before the major decompression at the bottom. For a 63-mm-long specimen, the propagation velocity of the signal corresponding to a transit time of 0.73 ms is 86 m/s. This value is much smaller than the p wave velocity measured by the ultrasonic test, 1000 m/s, or the decompression wave velocity, 730 m/s, in the specimen without bubbles.

[54] The velocity of a p wave, c_p^e, propagating in an elastic solid containing cylindrical bubbles in the direction perpendicular to the bubble axis is represented as

$$c_p^e = \sqrt{\frac{k_t^* + \mu_t^*}{\rho(1-\phi)}}, \tag{5}$$

where k_t^* and μ_t^* are the effective plane-strain bulk modulus and the effective shear modulus for the deformation in a plane perpendicular to the bubble axis, ρ is the density of the matrix without bubbles, and ϕ is the void fraction. The expression and bounds for k_t^* and μ_t^* are given by equations (A2), (A4), and (A5) in Appendix A, respectively.

[55] The solid and dashed curves in Figure 14 are the upper and lower bounds of the p wave velocity, c_p^e, calculated by equation (5). The bulk and the shear moduli of the compound determined by the ultrasonic measurement are used as K_m and μ_m. The isentropic modulus of the gas, γp_o, is used as K_p, where γ is the ratio of the heat capacity and p_o is the initial pressure of the specimen. The velocity of the observed precursor wave is marked by gray areas at the corresponding void fraction. The observation agrees well with the calculation.

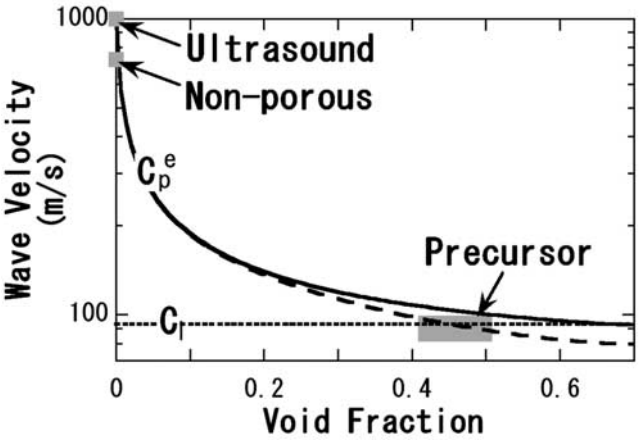

Figure 14. The velocity of the precursor signal obtained in the experiments is compared with theoretical values. The solid and dashed lines show the upper and the lower bounds of the p wave velocity propagating in an elastic solid containing cylindrical bubbles in the direction perpendicular to the bubble axis. The dotted line shows the longitudinal rod wave velocity of the compound without bubbles. The p wave velocity determined by the ultrasonic test and the decompression wave velocity measured in the nonporous specimen are shown by squares.

[56] Previous papers have reported the precursor phase of the pressure signal and assumed that its propagation velocity is $c_l = \sqrt{E_m/\rho}$, where $E_m = 9K_m\mu_m/(3K_m + \mu_m)$ is the Young's modulus of the matrix without bubbles [*Alidibirov and Panov*, 1998; *Alidibirov and Dingwell*, 2000]. This velocity is shown in Figure 14 by a dotted line and also agrees with the observation for the porous specimen. However, c_l does not account for the presence of the pores and the change of the wave velocity from the nonporous specimen to the porous one. From the physical standpoint, it is thus suggested that the equivalent elastic properties of the porous medium should be assessed to calculate the velocity of the elastic precursor wave.

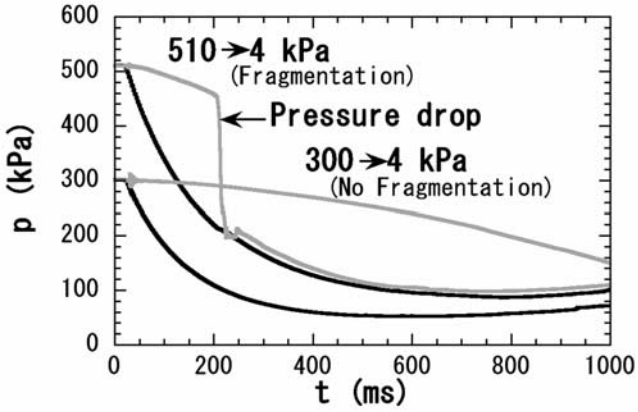

Figure 16. Pressure data obtained in the present experiment using an orifice with a fixed opening diameter of 3.16 mm. Corresponds with Figure 15. The gray lines represent the pressure measured at the base of the specimen, and the attached black lines represent the pressure above the specimen.

[57] Figure 15 shows the pressure data obtained by Spieler et al. (submitted manuscript, 2001) in the experiment using the real vesicular magma. The gray lines represent the pressure measured at the base of the specimen, and the attached black lines represent the pressure above the specimen. All the pressure data plotted in Figure 15 are obtained in a shock tube with a fixed geometry. Figure 16 is the corresponding plot obtained in the present experiment with fixed shock tube geometry and orifice diameter. In both figures, the sharp drop of the bottom pressure was observed with fragmentation and very slow decrease of the bottom pressure was observed without fragmentation. The

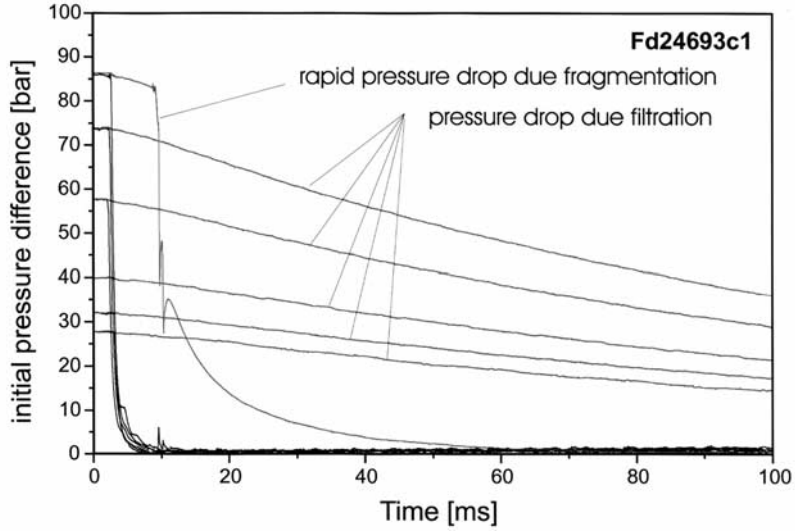

Figure 15. Pressure data obtained by Spieler et al. (submitted manuscript, 2001) in decompression experiments using real vesicular magma (dacite from Mount Unzen, Japan). The gray lines represent the pressure measured at the base of the specimen, and the attached black lines represent the pressure above the specimen.

direct observation of the behavior of the specimen demonstrated that the pressure history at the base of the specimen for the slower decompression rate (see Figure 11) exhibited a sharp drop (Figure 11c) well before rupture of the specimen occurred (Figures 11d–11f). This is in contrast with the assumption by Spieler et al. (submitted manuscript, 2001) that the observed pressure drop coincides with the onset of fragmentation. It is thus concluded that the pressure drop does not always occur simultaneously with fragmentation, and it can precede fragmentation due to the loss of contact between the specimen and the wall.

4.4. Implications to Magma Fragmentation

[58] The present experiments addressed the behavior of the porous viscoelastic specimen subjected to decompression. In the range of the elastic response of the viscoelastic specimen, the observations revealed features which were previously reported for the fragmentation of a porous solid [*Alidibirov and Panov*, 1998]. The fragmentation process was characterized by the following three observations. First, the fragmentation preceded expansion of the specimen. Second, fragmentation occurred with rupture surfaces perpendicular to the decompression axis. Third, the size of the fragments increased and the specimen tended to disrupt with a single rupture surface near the specimen base as the decompression condition was closer to the threshold. A similar fragmentation style has been assumed to occur in the experiments using vesicular magma for which plate-like fragments were collected upon completion of the decompression process [*Alidibirov and Dingwell*, 1996; *Martel et al.*, 2000; Spieler et al., submitted manuscript, 2001]. The present observations demonstrate for the first time that such a fragmentation style can actually occur in porous viscoelastic materials upon rapid decompression.

[59] The specimen disintegrated into several fragments and few fine particles were produced in the present experiment, while abundant fine ash is produced during an actual explosive eruption. We consider that the difference is not due to different mechanism or modes of fragmentation but due to different degree of fragmentation. It has been proposed that the fragmentation proceeds as a sequence of events [*Kaminski and Jaupart*, 1998; *Alidibirov and Dingwell*, 1996]. Primary breakup is considered to occur perpendicular to the decompression axis and generate relatively large fragments, which are then disintegrated to smaller particles [*Alidibirov and Dingwell*, 1996]. The secondary fragmentation may be caused by collisions and expansion of the remaining bubbles, and the final size distribution of the fragments depends on the time between primary fragmentation and eruption out of the vent [*Kaminski and Jaupart*, 1998]. It is also proposed that a certain amount of fine particles are produced at the primary fragmentation, and the amount seems to depend on the amplitude and the rate of decompression, the permeability of the specimen, and so on in a complicated way (O. Spieler, personal communication, 2001).

[60] Such a fragmentation style as observed in the present and other laboratory experiments is obviously affected by the one-dimensional stress field associated with geometry of the system. Although a volcanic system may be in a similar geometrical condition, a scaling law and description of the boundary effect must be established to apply the experimental results to the actual volcanic process.

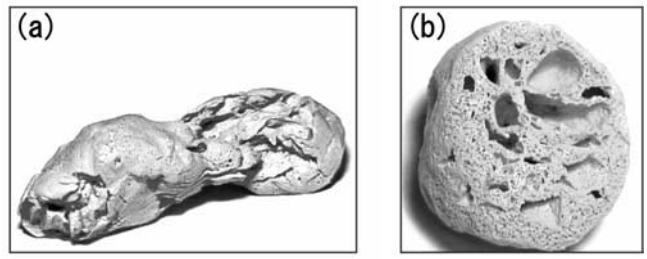

Figure 17. A fragment of (a) the specimen and (b) cross section.

[61] Finally, the product of our experiment and its cross section are presented in Figures 17a and 17b, respectively, even though they have been slightly altered during the extraction and processing following the experiment. The large pores are the remnants of the initial pores and the small bubbles are considered to have been produced by decompression.

[62] The experiments were not intended to construct a miniature volcano in the laboratory, but rather to clarify the underlying physics of magma fragmentation. Yet, it is felt that the present experiments bear marked similarities with natural magma fragmentation.

5. Conclusions

[63] Experiments were conducted on the dynamics of a porous viscoelastic material subjected to decompression. The following conclusions can be drawn from this study.

1. Brittle solid-like fragmentation and ductile expansion were both observed in the same porous material at different timescales.

2. Fragmentation occurs when the decompression exceeds a critical value (strength of the specimen) with a critical rate (characteristic timescale).

3. The critical time ($\sim$0.1 s) is very similar to both the measured glass transition time of the material (0.3 s) and the calculated timescale for the onset of viscous bubble expansion (0.1 s).

4. The typical pressure profile at the base of the specimen comprises a precursor wave related to the p wave velocity of the porous solid. It also exhibits a sharp drop which can actually indicate fragmentation or deformation of the specimen.

Appendix A: Effective Elastic Moduli of the Specimen

[64] The variational bounding method to estimate the effective moduli of composite material is outlined here. Assume that homogeneous strain is applied throughout a body of the composite material. Let the strain energy for this homogeneous field be denoted by $\tilde{U}^{\epsilon}$. The actual strain field of the composite body is not homogeneous. Let the strain energy for the actual strain field be denoted by U^{ϵ}. It follows from minimum potential energy that $U^{\epsilon} < U^{\epsilon}$. The effective elastic moduli are defined as the elastic moduli of a hypothetical homogeneous material which has the same potential energy as U^{ϵ} for the same boundary condition. The upper bounds for the effective elastic moduli are given by the rule

of minimum potential energy. To obtain a lower bounds, an appropriate homogeneous stress field is assumed throughout the body.

[65] The above method is used by *Hashin and Rosen* [1964] to derive bounds and expressions for the effective elastic moduli of materials reinforced by parallel hollow circular fibers. Their expressions are applicable to the present material containing parallel cylindrical pores by assuming the thickness of the fiber wall as zero. Bounds for the effective moduli relevant to the longitudinal wave perpendicular to the pore axes are obtained by assuming the strain and stress systems in the plane normal to the pore axes.

[66] The upper and the lower bounds for the plane-strain bulk modulus, k_t^*, agree with each other and the expression for k_t^* is explicitly given as

$$k_t^* = k_m + \frac{\phi}{\frac{1}{-k_m} + \frac{1-\phi}{k_m+\mu_m}}, \tag{A1}$$

where k_m and μ_m are the plane-strain bulk modulus and the shear modulus of the matrix without bubbles, respectively. Providing that the matrix consists of an isotropic material, $k_m = K_m + \frac{1}{3}\mu_m$, where K_m is the bulk modulus of the matrix without bubbles. Equation (A1) is obtained from equation (45) of *Hashin and Rosen* [1964] with the assumption of zero thickness of the fiber wall, and with correction of the misprint, $2\nu_b \rightarrow 1-2\nu$ [*Hashin and Rosen*, 1964].

[67] The expression for the solid fiber composite [*Hashin*, 1967] is useful in order to take account of the bulk modulus of the pore, K_p:

$$k_t^* = k_m + \frac{\phi}{\frac{1}{K_p-k_m} + \frac{1-\phi}{k_m+\mu_m}}. \tag{A2}$$

It is noted that $k_1 - k_2$ of Hashin should be corrected to $k_2 - k_1$, where k_1 and k_2 correspond to k_m and K_p, respectively. In a case that the matrix is fluid ($\mu_m = 0$), equation (A2) becomes

$$k_t^* = \frac{1}{\frac{\phi}{K_p} + \frac{1-\phi}{k_m}}, \tag{A3}$$

which agrees with the effective bulk modulus often used for the melt-gas mixture [e.g., *Mastin and Ghiorso*, 2000].

[68] The upper and the lower bounds for the effective shear modulus, $\mu_t^{*(+)}$ and $\mu_t^{*(-)}$, respectively, are

$$\mu_t^*(+) = \mu_m[1 - 2(1-\nu_m)A^\epsilon], \tag{A4}$$

$$A^\epsilon = \frac{2\phi(3-4\nu_m+\phi^3)}{3-4\nu_m+4(3-6\nu_m+4\nu_m^2)\phi-6\phi^2+4\phi^3+(3-4\nu_m)\phi^4},$$

$$\mu_t^{*(-)} = \mu_m/[1 + 2(1-\nu_m)A^\sigma], \tag{A5}$$

$$A^\sigma = \frac{2\phi(1+\phi+\phi^2)}{(1-\phi)^3},$$

where $\nu_m = (3K_m - 2\mu_m)/2(3K_m + \mu_m)$ is the Poisson ratio of the matrix. Equations (A4) and (A5) are obtained from equations (52) and (53) of *Hashin and Rosen* [1964] with the assumption of the zero thickness of the fiber wall.

[69] Although the bulk modulus of the gas is not included in the above formulation, its effect on the shear property is not considerable, which has been proved for the case of spherical inclusions [*Mavko et al.*, 1998].

[70] **Acknowledgments.** This work was supported by the Japan Society for the Promotion of Science. We thank O. Spieler and D. B. Dingwell for their helpful comments and providing us with their results (Figure 15). We are grateful to Y. Takei for help with the ultrasonic test, Rheometrics Scientific F. E. Ltd. for technical assistance with the rheometer test, and Dow Corning Corporation for providing us with the test material. T. Koyaguchi, E. E. Brodsky, and M. Kameda are acknowledged for the constructive discussions and encouragement throughout this study. Bradford Sturtevant passed away on 20 October 2000. M. Ichihara and D. Rittel dedicate this paper to his memory.

References

Alidibirov, M. A., A model for viscous magma fragmentation during volcanic blasts, *Bull. Volcanol.*, *56*, 459–465, 1994.

Alidibirov, M. A., and D. B. Dingwell, Magma fragmentation by rapid decompression, *Nature*, *380*, 146–148, 1996.

Alidibirov, M. A., and D. B. Dingwell, Three fragmentation mechanisms for highly viscous magma under rapid decompression, *J. Volcanol. Geotherm. Res.*, *100*, 413–421, 2000.

Alidibirov, M. A., and V. Panov, Magma fragmentation dynamics: experiments with analogue porous low-strength material, *Bull. Volcanol.*, *59*, 481–489, 1998.

Bennett, F. D., Vaporization waves in explosive volcanism, *Nature*, *234*, 538–539, 1971.

Cashman, K. V., B. Sturtevant, P. Papale, and O. Navon, Magmatic fragmentation, in *Encyclopedia of Volcanoes*, edited by H. Sigurdsson et al., pp. 421–430, Academic, San Diego, Calif., 1999.

Dingwell, D. B., Volcanic dilemma: Flow or blow?, *Science*, *273*, 1054–1055, 1996.

Dingwell, D. B., Recent experimental progress in the physical description of silicic magma relevant to explosive volcanism, in *The Physics of Explosive Volcanic Eruptions*, edited by J. S. Gilbert and R. S. J. Sparks, pp. 9–26, Geol. Soc., London, 1998.

Dingwell, D. B., and S. L. Webb, Structural relaxation in silicate melts and non-Newtonian melt rheology in geologic processes, *Phys. Chem. Miner.*, *16*, 508–516, 1989.

Eichelberger, J. C., and D. B. Hayes, Magmatic model for the Mount St. Helens blast of May 18, *J. Geophys. Res.*, *87*, 7727–7738, 1982.

Eisenberg, A., The glassy state and the glass transition, in *Physical Properties of Polymers*, 2nd ed., edited by J. E. Mark et al., pp. 61–95, Am. Chem. Soc., Washington, D. C., 1993.

Fink, J., and S. W. Kieffer, Estimate of pyroclastic flow velocities resulting from explosive decompression of lava domes, *Nature*, *363*, 612–615, 1993.

Graessley, W. W., Viscoelasticity and flow in polymer melts and concentrated solutions, in *Physical Properties of Polymers*, 2nd ed., edited by J. E. Mark et al., pp. 97–143, Am. Chem. Soc., Washington, D. C., 1993.

Hashin, Z., Theory of composite materials, in Mechanics of Composite Materials, edited by F. W. Wendt, H. Liebowitz, and N. Perrone, pp. 201–242, Pergamon, New York, 1967.

Hashin, Z., and B. W. Rosen, The elastic moduli of fiber-reinforced materials, *J. Appl. Mech.*, *31*, 223–232, 1964. (Hashin, Z., and B. W. Rosen, correction, *J. Appl. Mech.*, *32*, 219, 1965.)

Heiken, G., and K. Wohletz, *Volcanic Ash*, Univ. of Calif. Press, Berkeley, 1985.

Hill, L. G., An experimental study of evaporation waves in a superheated liquid., Ph.D. thesis, Grad. Aeronaut. Lab., Calif. Inst. of Technol., Pasadena, 1991.

Hill, L. G., and B. Sturtevant, An experimental study of evaporation waves in a superheated liquid, in *Adiabatic Waves in Liquid Vapor Systems*, edited by G. E. A. Meier and P. A. Thompson, pp. 25–37, Springer-Verlag, New York, 1990.

Howard, D. D., Exsolution of volatiles, Ph.D. thesis, Grad. Aeronaut. Lab., Calif. Inst. of Technol., Pasadena, 1996.

Kaminski, E., and C. Jaupart, The size distribution of pyroclasts and the fragmentation sequence in explosive volcanic eruptions, *J. Geophys. Res.*, *103*, 29,759–29,779, 1998.

Mader, H. M., Conduit flow and fragmentation, in *The Physics of Explosive Volcanic Eruptions*, edited by J. S. Gilbert and R. S. J. Sparks, pp. 51–71, Geol. Soc., London, 1998.

Mader, H. M., Y. Zhang, J. C. Phillips, R. J. S. Sparks, B. Sturtevant, and

E. Stolper, Experimental simulations of explosive degassing of magma, *Nature*, *372*, 85–88, 1994.
Martel, C., D. B. Dingwell, O. Spieler, M. Pichavant, and M. Wilke, Fragmentation of foamed silicic melts: An experimental study, *Earth Planet. Sci. Lett.*, *178*, 45–58, 2000.
Martel, C., D. B. Dingwell, O. Spieler, M. Pichavant, and M. Wilke, Experimental fragmentation of crystal- and vesicle-bearing silicic melts, *Bull Volcanol.*, *63*, 398–405, 2001.
Mastin, L. G., and M. S. Ghiorso, A numerical program for steady-state flow of magma-gas mixtures through vertical eruptive conduits, U.S Geol. Surv. Open File Rep., 00-209, 56 pp., 2000.
Mavko, G., T. Mukerji, and J. Dvorkin, *The Rock Physics Handbook*, Cambridge Univ. Press, New York, 1998.
Papale, P., Strain-induced magma fragmentation in explosive eruptions, *Nature*, *397*, 425–428, 1999.
Phillips, J. C., S. J. Lane, A. M. Lejeune, and M. Hilton, Gum rosin-acetone system as an analogue to the degassing behavior of hydrated magmas, *Bull. Volcanol.*, *57*, 263–268, 1995.
Prousevitch, A. A., D. L. Sahagian, and A. T. Anderson, Dynamics of diffusive bubble growth in magmas: Isothermal case, *J. Geophys. Res.*, *98*, 22,283–22,307, 1993.
Sato, H., T. Fujii, and S. Nakada, Crumbling of dacite dome lava and generation of pyroclastic flows at Unzen volcano, Japan, paper presented at IUGG XXI General Assembly, Boulder, Colo., 1995.
Sparks, R. S. J., The dynamics of bubble formation and growth in magmas: A review and analysis, *J. Volcanol. Geotherm. Res.*, *28*, 257–274, 1978.
Sparks, R. S. J., J. Barclay, C. Jaupart, H. M. Mader, and J. C. Phillips, Physical aspects of magmatic degassing, I, Experimental and theoretical constraints on vesiculation, *Rev. Mineral.*, *30*, 413–445, 1994.
Sugioka, I., and M. Bulsik, Explosive fragmentation of erupting magma, *Nature*, *373*, 689–692, 1995.
Taddeucci, J., and K. Wohletz, Temporal evolution of the Minoan eruption (Santorini, Greece), as recorded by its Plinian fall deposit and interlayered ash flow beds, *J. Volcanol. Geotherm. Res.*, *109*, 299–317, 2001.
Turcotte, D. L., H. Ockendon, J. R. Ockendorn, and S. J. Cowley, A mathematical model of vulcanian eruptions, *Geophys. J. Int.*, *103*, 211–217, 1990.
Webb, S. L., Silicate melts: Relaxation, rheology, and the glass transition, *Rev. Geophys.*, *35*, 191–218, 1997.
Webb, S. L., and D. B. Dingwell, The onset of non-Newtonian rheology of silicate melts: A fiber elongation study, *Phys. Chem. Miner.*, *17*, 125–132, 1990.
Wohletz, K. H., T. R. McGetchin, M. T. Sandford II, and E. M. Jones, Hydrodynamic aspects of caldera-forming eruptions: Numerical models, *J. Geophys. Res.*, *89*, 8269–8285, 1984.
Zhang, Y. X., Experimental simulations of gas driven eruptions: kinetics of bubble growth and effect of geometry, *Bull. Volcanol.*, *59*, 281–290, 1998.
Zhang, Y. X., A criterion for the fragmentation of bubbly magma based on brittle failure theory, *Nature*, *402*, 648–650, 1999.
Zhang, Y. X., and E. M. Stolper, Dynamics of gas-driven eruptions: Experimental simulations using CO_2–H_2O-polymer system, *J. Geophys. Res.*, *102*, 3077–3096, 1997.

M. Ichihara, Shock Wave Research Center, Institute of Fluid Science, Tohoku University, 2-1-1, Katahira, Aoba-ku, Sendai 980-8577, Japan. (mie@cc.tuat.ac.jp)

D. Rittel, Faculty of Mechanical Engineering, Technion, Israel Institute of Technology, Technion City, Haifa, 32000, Israel.